Intrazeolite Topotactic MOCVD. 3-Dimensional Structure-Controlled Synthesis of II–VI Semiconductor Nanoclusters

Geoffrey A. Ozin,* Mark R. Steele, and Andrew J. Holmes†

Advanced Zeolite Materials Science Group, Lash Miller Chemical Laboratories, University of Toronto, 80 St. George Street, Toronto, Ontario, Canada M5S 1A1

Received April 8, 1994[®]

A versatile synthetic method is described that blends conventional semiconductor chemistry with 3-D structure-controlled topotactic growth of semiconductor nanoclusters. The approach is utilized to assemble and organize II–VI semiconductor nanoclusters from MOCVD-type reagents within the diamond lattice of 13-Å spherical cavities found in zeolite Y. Specifically, these experiments involve the room-temperature reaction of volatile $(CH_3)_2M$ MOCVD reagents (where M = Zn, Cd) with Brønsted acid sites in $H_nNa_{56-n}Y$. This yields materials containing $ZOMCH_3$ (where ZO represents the zeolite oxide framework) MOCVD moieties anchored at α-cage (supercage) sites of zeolite Y. Exposure of $(CH_3M)_{48}Na_8Y$, containing six $ZOMCH_3$ MOCVD precursors per α-cage, to H_2X (where X = S, Se) induces a subsequent transformation to materials which analyze close to the ideal unit cell formula $(M_6X_4)_8H_{16}Na_8Y$. These are shown by a combination of IR, EXAFS, and Rietveld PXRD structure analyses to contain a diamond lattice of α-cage encapsulated $M_6X_4^{4+}$ nanoclusters. From the results of these analyses, an ideal structural model based on M_4X_4 cubane-type clusters, anchored through two of their chalcogenide vertices to the oxide framework of the zeolite by site II and III α-cage M^{2+} cations, namely, $M_2(M_4X_4)^{4+}$, is favored over an alternative $M_6X_4^{4+}$ adamantane geometry. Six $(CH_3)_2Cd$ species per α-cage can also be loaded into partially exchanged $H_nNa_{56-n}Y$ having n = 0, 8, 16, 24, 32, and 40. These react with, for example, H_2Se to yield nanoclusters of the type Cd_6Se_6 for n = 0, 8, $Cd_6Se_5^{2+}$ for n = 16, 24, 32 and $Cd_6Se_4^{4+}$ for n = 40. The latter is most similar to the $Cd_6Se_4^{4+}$ nanoclusters formed in the n = 48 zeolite host. The optical reflectance spectra of the $M_6X_4^{4+}$ nanoclusters display a blue shift of their absorption edges with respect to the bulk II–VI semiconductors, characteristic of quantum confinement. The order of the absorption edges of the II–VI nanoclusters, namely, $Zn_6S_4^{4+} > Zn_6Se_4^{4+} > Cd_6S_4^{4+} > Cd_6Se_4^{4+}$ follows that of the bandgap energies of the parent II–VI semiconductors. The luminescence emission and excitation profiles of the $Cd_6S_4^{4+}$ nanocluster have been studied over the 300–19 K temperature range. A 625-nm emission is proposed to originate from localized surface states associated with improperly terminated dangling bonds. The temperature dependence of the observed luminescence quenching of the 625-nm emission is consistent with a multiphonon radiationless relaxation process. This analysis yields an average mediating phonon frequency of 378 cm^{-1} and a Frank–Condon displacement parameter of 42.1 and supports an intermediate electron–phonon coupling case, all in accord with the model of a zeolite-anchored $Cd_2(Cd_4S_4)^{4+}$ nanocluster. A comparison is drawn between the process of depositing epitaxial layers of a II–VI semiconductor from MOCVD precursors on a 2-D planar substrate, with that of the intrazeolite topotactic stepwise assembly of a II–VI semiconductor nanocluster lattice on the 3-D curved internal surface of a zeolite.

Introduction

Structure-controlled semiconductor nanophysics and nanochemistry are providing new routes to quantum confined materials.[1,2] The goal of these efforts is to create perfect lattices built up of little pieces of bulk semiconductors, each bit restricted to nanometer sizes and having electrons confined in two, one, or zero dimensions. These nanostructures are known as quantum wells, wires, and dots, respectively. It is a major challenge to both synthesize and engineer, in a controlled and reproducible fashion, single-size and -shape materials in the nanoscale size regime. Materials that fall into this size domain, which have dimensions that lie between molecular and the bulk infinite lattices, show a mixture of classical and quantum mechanical traits. Electrons and holes in these structures display quantum size effects (QSE) and novel electronic and optical properties compared to the parent bulk semiconductor.[3,4] These are central to the development of new QSE electronic and optical devices and, ultimately, quantum circuitry.

Building in one and zero dimensions requires the development of a new generation of fabrication techniques

---

† Current address: Shell Research Limited, Thornton Research Centre, P.O. Box 1, Chester, England CH1 3SH.

[®] Abstract published in *Advance ACS Abstracts*, June 1, 1994.

(1) Reed, M. A. *Sci. Am.* **1993**, *1*, 118–123. Reed, M. A. *Science* **1993**, *262*, 195.

(2) Ozin, G. A. *Adv. Mater.* **1992**, *4*, 612–649; **1994**, *6*, 71–76 and references therein.

(3) Steigerwald, M. L.; Brus, L. E. *Acc. Chem. Res.* **1990**, *23*, 183–187 and references therein.

(4) Wang, Y. *Acc. Chem. Res.* **1991**, *24*, 133–139. Wang, Y.; Herron, N. *J. Phys. Chem.* **1991**, *95*, 525–532. Herron, N.; et al. *J. Am. Chem. Soc.* **1989**, *111*, 531.

0897-4756/94/2806-0999$04.50/0

able to achieve essentially perfect control over the size, shape, composition and purity of semiconductor nanostructures. This is important in order to minimize miniband energy level broadening arising from irregularities and defects introduced into the structures during the fabrication process.

From a nanophysics perspective,[1] recent reports show that lateral patterning of quasi-2-D heterostructures at the nanoscale level with lithographic methods creates size and shape inhomogeneities and defects, which when working in these dimensions, can dominate the electronic properties in a deleterious fashion. Several direct fabrication approaches to quantum dots and wires have been explored to overcome these problems. These include growth on tilted superlattices, growth on etched supersteps, and confinement induced by strain.[1] Their application has been limited so far because of the difficulty of continuously forming well-arranged steps. Two promising new approaches to overcome these difficulties involve direct synthesis of corrugated semiconductor superlattices and electrostatic squeezing of electrons in a buried quantum well layer.[1] The greatest challenge in both cases is still to achieve perfect, defect-free control over the dimensions of these nanostructures.

An appealing nanochemical approach to these kinds of structures involves the encapsulation of the components of bulk semiconductors inside a crystalline nanoporous material.[2–6] This is anticipated to improve their quantum performance by imposing strict uniformity of size, shape and organization. As the surfaces of semiconductor nanoclusters are usually highly reactive these clusters tend to spontaneously agglomerate. Various capping methods have been shown to effectively curtail the cluster growth problem.[3–5] Bare surfaces also contain improperly terminated dangling bonds which give rise to localized surface states, which tend to lie within the bandgap of the nanocluster. Surface capping can shift these surface states out of the bandgap, thereby removing effects that serve to deleteriously affect electron transport and electron–hole recombination processes.[5]

Zeolites are currently the only known crystalline nanoporous materials in which regularly repeating arrays of semiconductor nanoclusters have been assembled.[2–6] With access to large-cavity (e.g., faujasite), extra-large-cavity (e.g., cloverite, JDF-20) and mesoporous materials (e.g., MCM-41), for example, it should now prove possible to create semiconductor nanocluster lattices with tunable individual cluster sizes in the 10–200-Å range.[2–6] Achieving perfect three-dimensional atomic scale control still remains a synthetic challenge. Capping techniques that have proven useful for synthesizing and stabilizing nanometer scale semiconductors have included the use of micelles, polymers, porous glasses, polypeptides, oxide coatings and simple alkyl and aryl ligands.[2,5] "Zeolate" capping can be considered to be a natural extension of these methods.[2,7] Spatial templating constraints, steric restrictions, and charge-balance considerations imposed by the zeolite host provide control over the size, shape, and spatial homogeneity of constituent semiconductor nanoclusters. One promising approach involves synthetic methods that creatively blend conventional semiconductor technology with three-dimensional structure-controlled topotactic growth of semiconductor nanoclusters. As a step in this direction, the goal of this study is to explore in some detail the use of MOCVD-type reagents for the self-assembly and organization of II–VI semiconductor nanoclusters inside the diamond lattice of 13-Å α-cages (supercages) found in zeolite Y. A communication describing this approach for III–V gallium phosphide nanoclusters in zeolite Y has been reported.[8] The details of II–VI MOCVD precursor anchoring have also been described recently.[9] Intrazeolite II–VI nanoclusters were first synthesized in the β-cages of zeolite Y by an aqueous-phase method.[4]

Experimental Section

Chemicals. Electronic grade $(CH_3)_2Zn$ and $(CH_3)_2Cd$ (99.999%, Strem) and voltaic grade H_2Se (99.999%, Scott Specialty Gas) were used as supplied. Hydrogen sulfide (99.5%, Matheson) was further purified by passing the gas through a molecular sieve filter to remove trace amounts of water. Research grade sodium zeolite Y (lot number 130-76-81, analyzed as $Na_{56}Y$) was kindly donated by Dr. Edith Flanigen of Union Carbide-UOP, Tarrytown, NY.

Synthesis. NH_4Y was prepared by a three-step process: (i) defect removal by slurring NaY in 0.1 M NaCl, followed by thorough washing with distilled, deionized water; (ii) shallow bed calcination in a flow through reaction chamber; (iii) batch ion-exchange(s) in 0.1 M NH_4Cl, to produce a specific level of ammonium loading, washing with copious amounts of distilled deionized water between each exchange. Samples denoted $(NH_4)_nNa_{56-n}Y$ with n = 8, 16, 24, 32, 40, and 48 were prepared.

Ammonium exchanged zeolite Y was pressed into a thin wafer which was placed in a cell, designed to allow *in situ* spectroscopic observation and then dehydrated and deamminated using a furnace with a preset temperature ramping program: 25–100 °C over 2 h, hold at 100 °C for 2 h, ramp from 100 to 430 °C over 4 h and hold at 430 °C for 2 h. The resulting samples were white. The mid-IR spectra reveal diagnostic νOH_α (3636 cm^{-1}) and νOH_β (3546 cm^{-1}) stretching frequencies of α- and β-cage (supercage and sodalite cage) Brønsted acid sites. Their relative intensities depended on the level of NH_4^+ ion exchange in the parent $(NH_4)_nNa_{56-n}Y$. Dimethylcadmium $(CH_3)_2Cd$ (vapor pressure 28 Torr at 20 °C) or dimethylzinc $(CH_3)_2Zn$ (vapor pressure 306 Torr at 20 °C) was added to the zeolite wafer from a bulb reservoir attached to the *in situ* cell. The room temperature reaction was monitored by *in situ* mid-IR spectroscopy. In this way, α- and β-cage Brønsted acid sites were quantitatively titrated with $(CH_3)_2M$ to produce the anchored, extraframework charge-balancing, species denoted $ZOMCH_3$ with characteristic νCH frequencies. Details of this anchoring process have been described in an earlier publication from this laboratory.[9] The CH_4 byproduct was expelled from the hydrophilic zeolite Y host and was conveniently quantified in the gas phase of the *in situ* cell by mid-IR spectroscopy. The loss of Brønsted acid sites was found to be directly proportional to the amount of evolved CH_4. The Brønsted acid sites were partially or wholly titrated with $(CH_3)_2M$. These $ZOMCH_3$ anchored MOCVD samples could then be reacted with gaseous H_2S or H_2Se to form II–IV semiconductor nanoclusters housed inside the zeolite Y host. In this cluster self-assembly reaction, CH_4 was again evolved and quantified. The number of Brønsted acid sites reinstated in the zeolite by this process, together with elemental analyses, provided quantitative information on the composition and charge of the imbibed cluster.

Mid-IR Spectroscopy. Mid-IR spectra were recorded on self-supporting wafers of zeolite Y mounted within an *in situ* reaction

---

(5) Brus, L. E. *Adv. Mater.* **1993**, *5*, 286 and references therein.

(6) Stucky, G. D.; MacDougall, J. E. *Science* **1990**, *247*, 669–678. Ozin, G. A.; Kuperman, A.; Stein, A. *Angew. Chem., Int. Ed. Engl.* **1989**, *28*, 359–376 and references therein.

(7) Ozin, G. A.; Özkar, S. *Chem. Mater.* **1992**, *4*, 511–521. Steele, M. R.; Holmes, A. J.; Ozin, G. A. *Proc. 9th IZA* **1993**, *2*, 185–192. Ozin, G. A.; Bowes, C. L.; Steele, M. R. *Mater. Res. Soc. Ser.* **1992**, *277*, 105–112. Ozin, G. A.; Bowes, C. L. *Mater. Res. Soc. Symp. Proc.* **1993**, *286*, 93.

(8) MacDougall, J. E.; Eckert, H.; Stucky, G. D.; Herron, N.; Wang, Y.; Moller, K.; Bein, T.; Cox, D. *J. Am. Chem. Soc.* **1989**, *111*, 8006–8008.

(9) Steele, M. R.; Macdonald, P. M.; Ozin, G. A. *J. Am. Chem. Soc.* **1993**, *115*, 7285–7292. Ozin, G. A.; Steele, M. R. *Adv. Mater.* **1994**, *6*, 300–303.

cell having NaCl (4000–400 cm^{-1}) windows. A Nicolet 20SXB spectrometer was used to collect mid-IR spectra of the samples at a resolution of 2 cm^{-1}. FT-IR spectra were collected by coadding 32 interferograms.

UV-Visible Diffuse Reflectance Spectroscopy. Measurements were obtained using a Perkin-Elmer 330 spectrophotometer adapted with an integrating sphere and linked to a computer to digitize the data. Spectra were collected in an *in situ* cell and referenced with respect to $BaSO_4$. Diffuse reflectance spectra were transformed to absorption spectra by use of the Kubelka–Munk equation:

$$K/S = (1 - R)^2/2R$$

R is the relative diffuse reflectance defined as: $R = R(\text{sample})/R(\text{reference})$, K is the molar absorption coefficient and S is the scattering coefficient. The latter is independent of wavelength if the size of the scattering zeolite particles (about 1–10 μm) are large in relationship to the wavelength used (0.2–0.8 μm).[10]

Luminescence Spectroscopy. Steady-state photoluminescence spectra were recorded using a 450-W xenon arc lamp (Osram XBO, Oriel Corp.) as the excitation source. The output of the lamp was collected by a spherical reflector, focused with a condensing lens, passed through a 10-cm water-cooled IR filter, and refocused onto the monochromator with a UV grade fused silica lens. Excitation and emission profiles were obtained using 0.2-m monochromators (300-nm or 500-nm blazing, Photon Technology International) and various bandpass (Schott) and cutoff (Ealing) filters. Photons were detected using a Hamamatsu R928 PMT in a water-cooled PRA International holder. The high voltage for the emission PMT was supplied by a Pacific Precision Instruments Model 124 power supply operating at 1250 V. The anode output from the PMT was amplified with an EG&G Ortec 9305 fast preamplifier. The counting electronics consisted of a Tracor Northern (TN7200) multichannel analyzer in multichannel scaling mode. Spectra were corrected for the quantum sensitivity profile of the PMT (supplied by Hamamatsu Corp. for a typical R928 PMT), filter, and lamp intensity profiles (as recorded experimentally). The sample was placed as a wafer inside an *in situ* cell with fused silica windows that was evacuated to 10^{-7} Torr and cooled to 15–20 K (monitored using a calibrated chromel versus gold thermocouple) using a closed-cycle helium refrigerator (Air Products Model CS 202 Displex). The sample temperature was varied by use of a heater attached to the tip of the cryostat.

EXAFS Spectroscopy. EXAFS data were collected at the National Synchrotron Light Source on beamlines X11A and X23A2 at Brookhaven National Laboratory. The X-ray energy was tuned to the nucleus of choice and calibrated with a foil of the respective bulk element. The monochromator was then detuned 10–30% to remove contributions from the second harmonic of the X-ray beam. Incident and transmitted beams were detected with gas-filled ion chambers tuned to absorb 10% and 80% of the X-ray photons respectively. Samples were prepared in an inert atmosphere, mixing a quantity of material calculated to give an absorbance of 1.5 with a 2:1 wt % mixture of hexadecane:octacosane and then packed into aluminum sample holders. The samples were then sealed with Kapton windows and mounted in a liquid nitrogen cooled cryostat to perform the EXAFS measurements. Data analysis was carried out as follows: The initial spectra were plotted as $\ln(I_0/I)$ versus energy in electronvolts. The zero point was then chosen as the half-height of the absorption. The data were then converted to k space, truncated to extract the EXAFS signal, the background removed using a spline function and then Fourier transformed to r space. Coordination shells were then filter extracted, back-transformed and fitted relative to parameters extracted from EXAFS spectra of suitable reference materials (CdO, CdS, CdSe, ZnS, ZnSe) using a least-squares algorithm to fit the bond length, coordination numbers, inner potential and Debye–Waller factors of the sample.

Rietveld PXRD Structure Refinement. Low-temperature, high-resolution powder diffraction data were collected on beamline X7A at the Brookhaven National Synchrotron Light Source. Data collection utilized 0.7051-Å radiation (calibrated using a Si standard). Intensity was scaled to the ring current of the Synchrotron source using an ion prechamber to monitor the intensity of the incident beam. A Kevex detector was used to monitor the diffracted X-rays. Step intervals of 0.01° 2θ and integration times ranging from 6 to 10 s were used to collect diffraction patterns. Samples were rocked at 2° to maximize particle statistics. Further information on the experimental setup is described in detail elsewhere.[11] Samples were sealed in Lindemenn tubes, which were cooled to 15 K. Rietveld analysis was accomplished using GSAS structural analysis software.[12] Peak shapes were modeled using a pseudo-Voigt function. The location of extraframework atoms were determined by refining their positions as located in Fourier maps after initial refinement of the zeolite host structure. The progress of the refinement was monitored using wRp, Rp and χ^2.

Table 1. Chemical Analysis of Samples

sample	composition of extraframework guests per supercage[a]
HY	$Na_{1.0(1)}H_{6.0}Y$
CdS–Y	$Cd_{5.5(3)}S_{4.2(7)}Y$
CdSe–Y	$Cd_{5.0(4)}Se_{4.0(5)}Y$
ZnS–Y	$Zn_{5.3(9)}S_{3.6(7)}Y$
ZnSe–Y	$Zn_{5.4(9)}Se_{3.8(4)}Y$

[a] Errors in parentheses calculated from the standard deviations of the elemental analyses as supplied by Galbraith Laboratories.

Elemental Analysis. Elemental analyses were performed by Galbraith Laboratories. Inductively-coupled plasma emission spectroscopy (ICP) was used to analyze for Si, Al, Na, Cd, Zn, S, and Se. These results demonstrated that II–VI clusters which analyze close to $M_6X_4^{4+}$ per supercage (for M = Zn, Cd; X = S, Se) could be formed in the fully loaded $H_{48}Na_8Y$ host; see Table 1.

Results and Discussion

In this paper we describe a mild, controlled, clean and versatile method for reacting volatile MOCVD species such as $(CH_3)_2Zn$ and $(CH_3)_2Cd$ with Brønsted acid sites in $H_nNa_{56-n}Y$. This quantitatively yields anchored $ZOZnCH_3$ and $ZOCdCH_3$ moieties located at specific sites in the α-cages of zeolite Y.[9] These intrazeolite MOCVD-type precursors are perfectly poised and appropriately located for topotactic self-assembly reactions with gaseous H_2S and H_2Se reagents, to form II–VI semiconductor nanoclusters uniformly distributed within the diamond network of 13-Å α-cages of the host zeolite.

Adsorption of Hydrogen Chalcogenides. The study of H_2S in zeolites has been extensive owing to the technological importance of zeolites as catalysts in the oxidation of H_2S by O_2 or air to sulfur, the Claus reaction between H_2S and SO_2 to recover sulfur from sour gas streams and the detection of atmospheric H_2S.[13] Earlier work on the adsorption of H_2S in faujasite shows charge separation and ionization processes involving the extraframework Na^+ cations in aluminous NaX at low coverage to be complete:

$$2ZO + ZONa + H_2S \rightarrow ZONaS + 2ZOH$$

and at high coverage to be partial:

---

(10) Frei, R. W.; MacNeil, J. D. *Diffuse Reflectance Spectroscopy in Environmental Problem Solving*; CRC Press: Akron, 1973.

(11) Cox, D. E.; Toby, B. H.; Eddy, M. M. *Aust. J. Phys.* **1988**, *41*, 117–131.

(12) Rietveld refinement, using the Generalized Structure Analysis System, provided by A. C. Larson and R. B. Von Dreele, LANSCE, Los Alamos National Laboratories.

(13) Lee, H. *Adv. Chem. Ser.* **1973**, *111*, 311. Addison, W. E.; Walton, A. *J. Chem. Soc.* **1961**, 4741. Street, Jr., K. W.; Mark, Jr., H. B.; Vasireddy, S.; LaRue-Filio, R. A.; Anderson, C. W.; Fuller, M. P.; Simon, S. J. *J. Appl. Spectrosc.* **1985**, *39*(1), 68–72.

$$\mathrm{ZO + ZONa + H_2S \rightarrow ZONaSH + ZOH}$$

In the more siliceous NaY these dissociation processes are not observed, and instead molecular adsorption occurs involving Na^+ cation and oxygen framework sites.

With H_2S in HY, selective hydrogen-bonding between α-cage Brønsted acid sites occurs:

$$\mathrm{ZOH_\alpha + H_2S \rightarrow ZOH_\alpha{\cdots}SH_2}$$

This phenomenon is manifest in the mid-IR spectrum as an intense broad bathochromically shifted absorption ($\Delta\nu \approx 510\ \mathrm{cm^{-1}}$) around 3130 $\mathrm{cm^{-1}}$, which gradually replaces the νOH_α band with increased loading of H_2S. An illustration of this kind of ZOH_α/H_2S titration is shown in Figure 1. This adsorption process can be completely reversed by evacuating the sample at 100 °C. The adsorption of H_2Se in HY is similar to that of H_2S in HY. The main difference is the observation of a less bathochromically shifted $\nu OH_\alpha{\cdots}SeH_2$ absorption ($\Delta\nu \approx 470\ \mathrm{cm^{-1}}$) around 3170 $\mathrm{cm^{-1}}$ compared to $\nu OH_\alpha{\cdots}SH_2$, most likely due to the weaker hydrogen bonding of H_2Se relative to H_2S in HY. Similar effects were found in an analogous study of HX (X = Cl, Br, I) molecules adsorbed in HY.[14]

MOCVD Precursor Anchoring. The intrazeolite MOCVD anchoring chemistry using $(CH_3)_2M$ reagents (where M = Zn, Cd) can be described in a general form by the following reaction stoichiometry:

$$\mathrm{H_{\mathit{n}}Na_{56-\mathit{n}}Y + 48(CH_3)_2M \rightarrow \mathit{n}[CH_3M](48-\mathit{n})[(CH_3)_2M]Na_{56-\mathit{n}}Y + \mathit{n}CH_4} \quad (1)$$

The faujasite host is obtained by using standard ammonium ion-exchange of $Na_{56}Y$ followed by a vacuum thermal deammination procedure. The reactivity (nucleophilicity) of the methyl substituents of gaseous $(CH_3)_2M$ are sufficiently high to allow reaction with both α- and β-cage Brønsted acid sites at room temperature. The steric demands of $(CH_3)_2M$, however, are such that anchoring of $ZOMCH_3$ and chemisorption of $(CH_3)_2M$ is restricted to α-cage site locations. The reaction is quantitative and can be conveniently probed by *in situ* mid-IR spectroscopy using self-supporting wafers of the $H_nNa_{56-n}Y$ host. The extent of anchoring to the protons is defined by the simultaneous monitoring of (i) the decrease of νOH_α and νOH_β Brønsted acid site IR intensity and (ii) the concomitant growth of the νCH mode intensity of the anchored $ZOMCH_3$ guest, chemisorbed $(CH_3)_2M$ and CH_4, the latter observed in the gas phase of the *in situ* cell. Excess physisorbed $(CH_3)_2M$ moieties introduced into the α-cage during this process can be conveniently reduced to zero following evacuation of the sample at room temperature. This procedure locates a total of six oxide framework anchored $ZOMCH_3$ and chemisorbed $(CH_3)_2M$ moieties per α-cage over the composition range $0 \leq n \leq 48$ used in this study.[9] Mid-IR spectra depicting this process for various values of n = 0, 8, 16, 24, 32, 40, and 48 of six $(CH_3)_2Cd$ MOCVD precursors per α-cage are shown in Figure 2. Because the νCH stretching modes of the methyl groups of anchored $ZOMCH_3$ and chemisorbed $(CH_3)_2M$ occur at slightly different frequencies, it is possible to distinguish the relative proportions of these two species over this compositional regime. Analysis of these mid-IR spectra reveal a proportional relationship between the two contributing species. That is, anchored $ZOMCH_3$ monotonically increases as chemisorbed $(CH_3)_2M$ decreases with higher values of n, while maintaining the total number of metal species at six per α-cage (Figure 2).

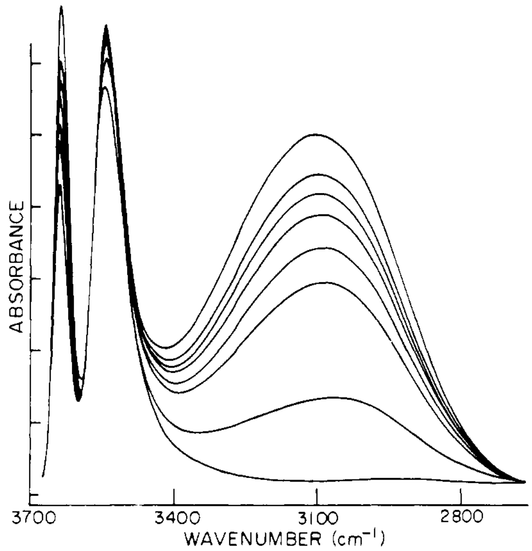

Figure 1. Mid-IR spectra of H_2S adsorbed into $H_{48}Na_8Y$. The α-cage protons (νOH_α = 3636 $\mathrm{cm^{-1}}$) are increasingly solvated and bathochromically shifted to 3130 $\mathrm{cm^{-1}}$ as more H_2S is added.

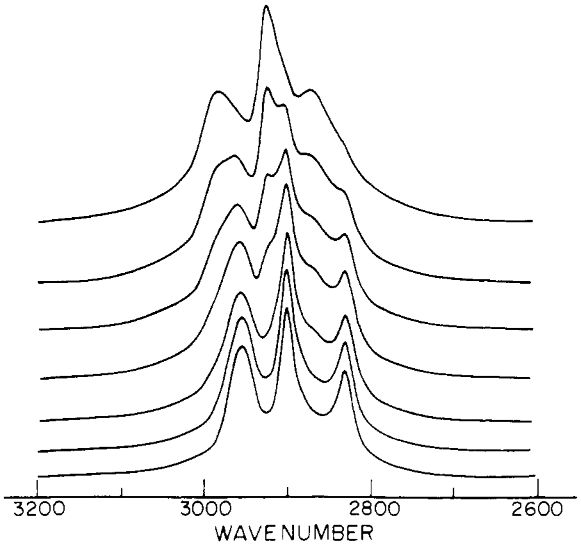

Figure 2. Mid-IR spectra showing νCH stretching bands of anchored $ZOCdCH_3$ and chemisorbed $(CH_3)_2Cd$ in $H_nNa_{56-n}Y$. From bottom to top n = 0, 8, 16, 24, 32, 48.

A straightforward extension of the above described procedure allows any degree of anchoring of $ZOMCH_3$ in the α-cage of zeolite Y, as exemplified by the $H_{48}Na_8Y$ host and described by the following reaction stoichiometry:

$$\mathrm{H_{48}Na_8Y + \mathit{m}(CH_3)_2M \rightarrow \mathit{m}[CH_3M]H_{48-\mathit{m}}Na_8Y + \mathit{m}CH_4} \quad (2)$$

This is simply achieved by stopping a mid-IR monitored titration of Brønsted acid sites with $(CH_3)_2M$ at a specified loading value. A representative collection of spectral traces depicting this process is shown in Figure 3. Moreover, the reaction can be initiated with, for example, $(CH_3)_2Zn$ and completed by $(CH_3)_2Cd$, to yield specific mixtures of α-cage

---

[14] Ozin, G. A.; Özkar, S.; McMurray, L. *J. Phys. Chem.* **1990**, *94*, 8297–8302.

[15] Garbowski, E. D.; Mirodatos, C. *J. Phys. Chem.* **1982**, *86*, 97.

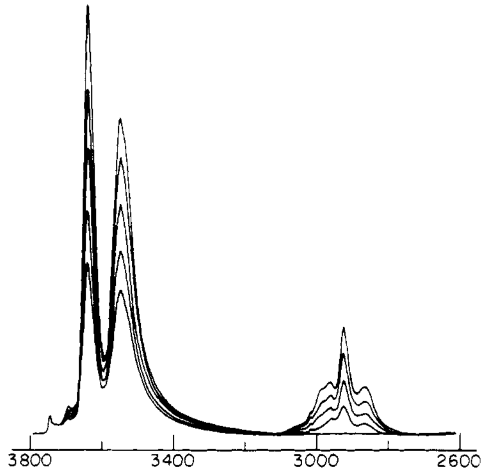

Figure 3. Mid-IR spectra of the titration of charge balancing α- and β-cage protons in $H_{48}Na_8Y$ with $(CH_3)_2Cd$. The decreasing intensity of the $\nu OH_{\alpha,\beta}$ stretching bands (3636, 3546 cm^{-1}, respectively) of the zeolite Brønsted acid sites is accompanied by a concomitant increase in that of the νCH stretching bands (2958, 2900, 2834 cm^{-1}) of the charge-balancing $ZOCdCH_3$ moieties.

anchored $ZOZnCH_3$ and $ZOCdCH_3$ MOCVD type precursors. This allows access to both single and binary component II–VI semiconductor nanoclusters in the host zeolite with any desired ratio of metal and chalcogenide.

In an earlier study, we established by Rietveld PXRD structure refinement that samples of $(CH_3M)_{44}Na_{12}Y$ for M = Zn, Cd, contain close to six $ZOMCH_3$ moieties exclusively anchored at α-cage sites in the zeolite Y host lattice.[9] It was found that there are roughly equal numbers of $ZOMCH_3$ species anchored at crystallographic cation sites II and III. The former reside over 6-ring sites within the α-cage, while the latter are located in the 12-ring entrance windows to the α-cage, thereby modifying the free diameter (space) available for the passage of H_2S and H_2Se reagents into the α-cage. With four tetrahedrally-arranged 12-ring windows and six $ZOMCH_3$ per α-cage, there is, on average, one to two site III $ZOMCH_3$ species partially blocking the 12-ring aperture to the α-cage. The reaction of the anchored $ZOMCH_3$ species with H_2S is rapid and complete for both M = Zn, Cd at any loading value in the range $0 < m < 48$. Reaction with H_2Se is also spontaneous at room temperature with the zinc samples at all points in the range $0 < m < 48$. In sharp contrast for cadmium samples, no reaction occurs at room temperature for $m > 45$. Below this value of m, reaction with H_2Se is again spontaneous at room temperature. Only by warming the $m > 45$ sample to 200 °C can one induce reaction. With respect to the conditions required to induce reaction between anchored $ZOMCH_3$ and H_2S/H_2Se reagents, it is clear that the 12-ring blocking properties of site III $ZOMCH_3$ species can distinguish H_2S and H_2Se, differing in kinetic diameter by around 0.2 Å. The origin

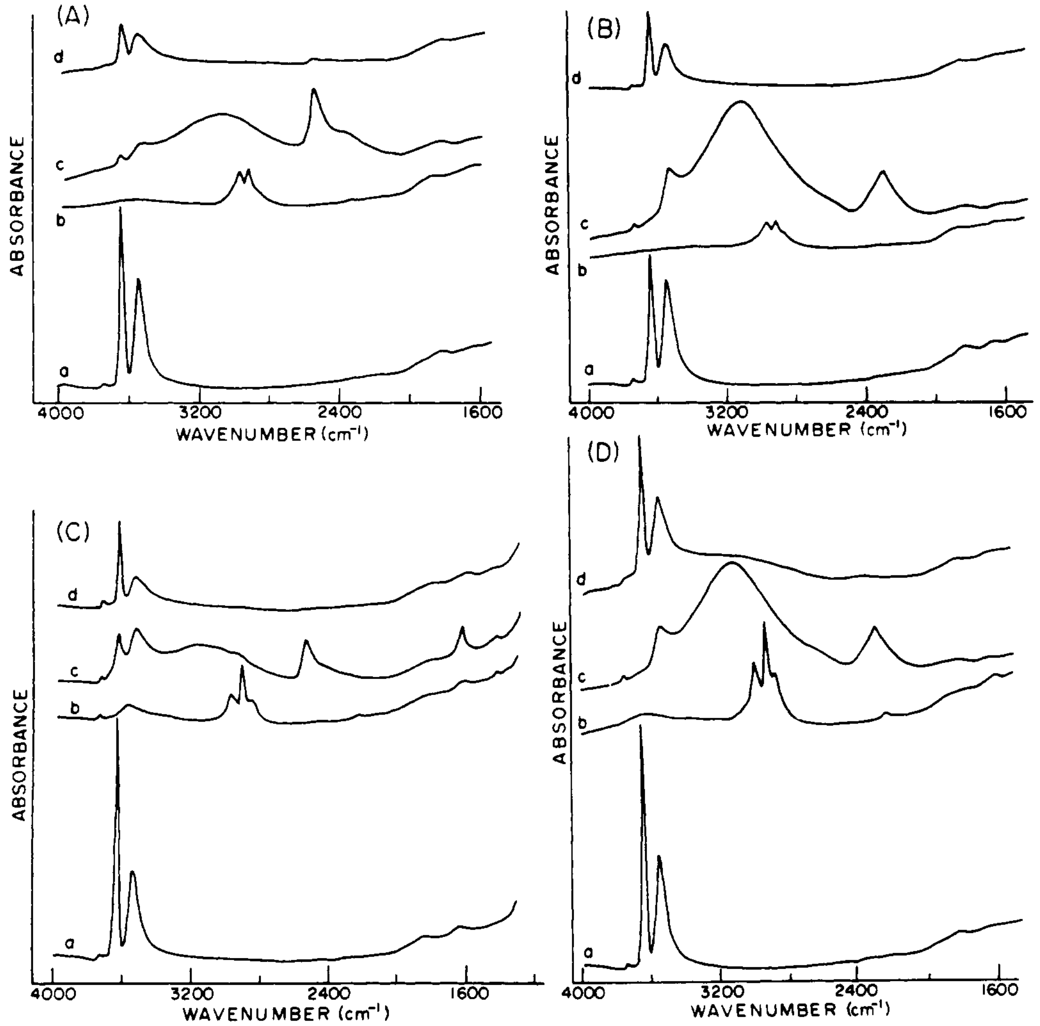

Figure 4. Mid-IR spectra depicting the formation of α-cage $M_6X_4^{4+}$ clusters: (A) $Zn_6S_4^{4+}$, (B) $Zn_6Se_4^{4+}$, (C) $Cd_6S_4^{4+}$, (D) $Cd_6Se_4^{4+}$. Spectra correspond to (a) $H_{48}Na_8Y$ host, (b) the $ZOMCH_3$ precursor, (c) addition of H_2X, and (d) the $M_6X_4^{4+}$ cluster product.

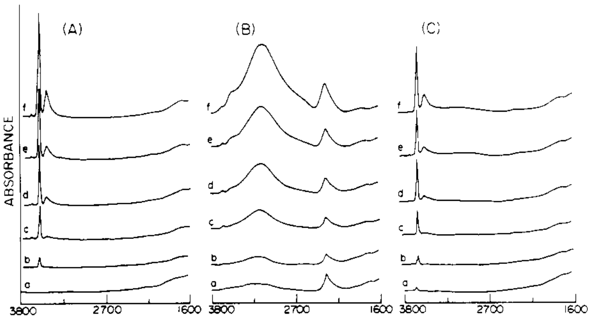

Figure 5. Mid-IR spectra depicting the formation of $Cd_6Se_{6-x}^{2x+}$ clusters in $H_nNa_{56-n}Y$: (A) dehydrated hosts; (B) addition of H_2Se; (C) the $Cd_6Se_{6-x}^{2x+}$ cluster product. Spectra a–f correspond to samples with $n = 0, 8, 16, 24, 32, 48$.

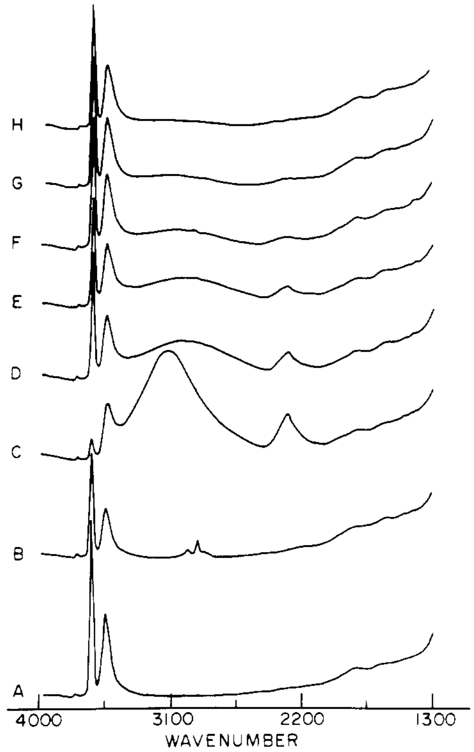

Figure 6. Mid-IR spectra depicting the formation of cadmium selenide clusters evolving from partially titrated $n(CH_3Cd)H_{48-n}Na_8Y$: (A) the $H_{48}Na_8Y$, $n = 0$ host; (B) $n = 37$; (C) addition of H_2Se to sample (B); (D–H) evacuation of H_2Se at 25, 50, 100, 150, 200 °C.

of this molecular discrimination effect is described elsewhere.[9]

Cluster Self-Assembly. The intrazeolite II–VI semiconductor nanocluster self-assembly chemistry can be described by the following general reaction scheme for the full loading condition of six $(CH_3)_2M$ MOCVD precursors per α-cage:

$$n[CH_3M](48-n)[(CH_3)_2M]Na_{56-n}Y + (48-8x)H_2X \rightarrow [M_6X_{6-x}]_8H_{n-16x}Na_{56-n}Y + (96-n)CH_4 \quad (3)$$

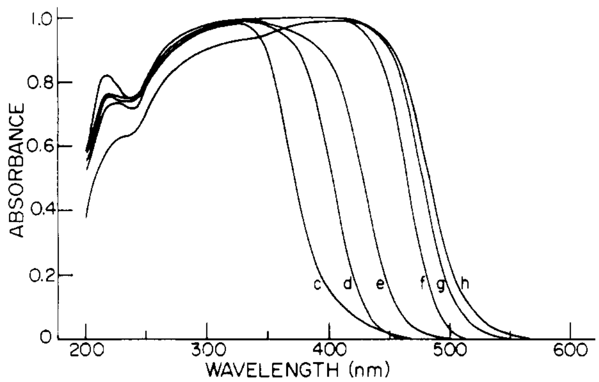

Figure 7. Red shifting absorption edge depicting the formation of cadmium selenide clusters evolving from partially titrated $n(CH_3Cd)H_{48-n}Na_8Y$ where (c–h) correspond to the same samples of Figure 6.

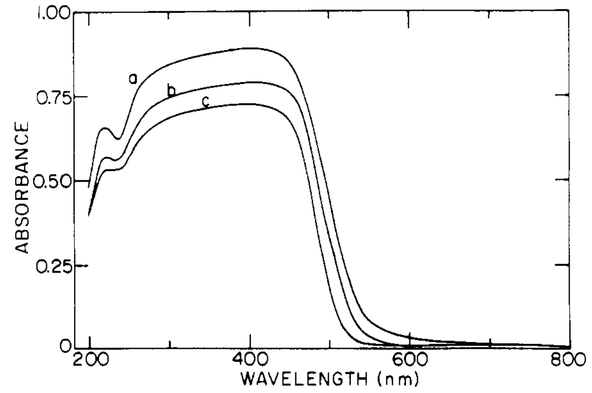

Figure 8. Optical absorption edges of cadmium selenide cluster products resulting from the reaction of H_2Se with $n(CH_3Cd)H_{48-n}Na_8Y$, where (a) $n = 6.3$, (b) $n = 19.2$, and (c) $n = 45.1$.

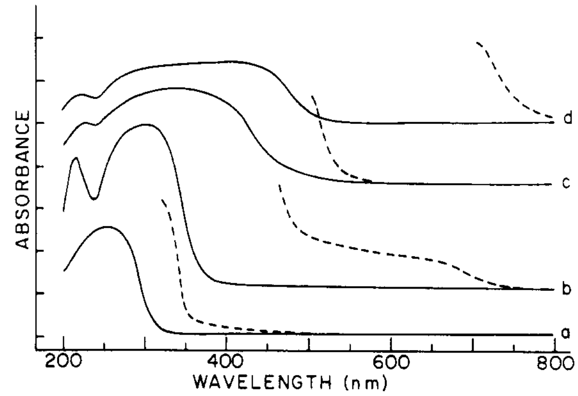

Figure 9. UV–visible reflectance spectra (—) of $M_6X_4^{4+}$ clusters formed in the $H_{48}Na_8Y$ host, relative to those of their bulk semiconductor counterparts (- - -) (a) M = Zn, X = S; (b) M = Zn, X = Se; (c) M = Cd, X = S; (d) M = Cd, X = Se.

The progress and stoichiometry of this reaction was monitored by *in situ* mid-IR spectroscopy and quantified from a knowledge of the initial population of α- and β-cage Brønsted acid sites, the fraction of Brønsted acid sites reinstated, the amount of gaseous CH_4 evolved into the reaction cell, and the elemental analysis of the final cluster product. A collection of representative mid-IR spectral traces depicting this cluster self-assembly reaction for $n = 48$ systems is shown in Figure 4. The cluster self-assembly, as depicted by mid-IR, for the M = Cd, X = Se system for samples with $n = 0, 8, 16, 24, 32, 40$, and 48 is shown in Figure 5. Analysis of these materials by PXRD reveal that crystallinity and integrity of the zeolite Y host is maintained with no sign of diffraction peaks characteristic of the bulk II–VI material. SEM results show no evidence of compositional gradients nor outer coating of the crystals with bulk II–VI material. These results indicate that the II–VI semiconductor nanocluster self-assembly reactions take place predominantly within the confines of the zeolite Y host according to the reaction

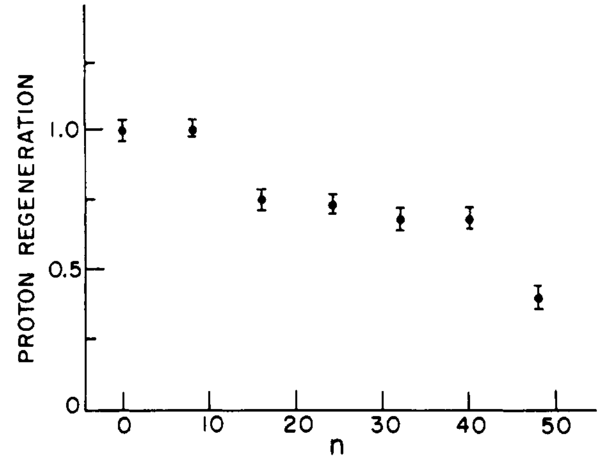

Figure 10. Plot of the extent of proton regeneration versus n, for the formation of $Cd_6Se_{6-x}{}^{2x+}$ in the $H_nNa_{56-n}Y$ host, corresponding to the samples shown in Figure 5.

Table 2. EXAFS Data Analysis for $M_6X_4{}^{4+}$ II–VI Semiconductor Nanoclusters in Zeolite Y, Where M = Zn, Cd; X = S, Se

sample	shell[a]	R (Å)	N_{obs}	N_{cube}	N_{adam}	$\Delta\sigma^2$ (Å^2)	ΔE_0 (eV)
CdS	**Cd**–O	2.24	1.39	1.00[b]	0.50[c]	0.0054	0.95
	Cd–S	2.52	2.25	2.33	2.00	0.0037	0.23
CdSe	**Cd**–O	2.23	1.58	1.00	0.50	0.0048	2.2
	Cd–Se	2.60	2.98	2.33	2.00	0.0051	−1.0
	Cd–**Se**	2.59	2.92	3.50	3.00	0.0026	0.99
ZnS	**Zn**–O	1.95	1.00	1.00	0.50	0.00001	3.3
	Zn–S	2.30	2.40	2.33	2.00	0.00034	2.1
ZnSe	**Zn**–O	2.04	1.07	1.00	0.50	−0.0019	0.74
	Zn–Se	2.43	3.32	2.33	2.00	0.0026	−3.2
	Zn–**Se**	2.41	3.41	3.50	3.00	0.0025	1.0

[a] Bold lettering indicates K-edge probed. [b] Tethering of two M^{2+} to site II and III for $M_2(M_4X_4)^{4+}$ cubane structure (see text). [c] Tethering of one M^{2+} to site II for $M_6X_4{}^{4+}$ adamantane structure (see text).

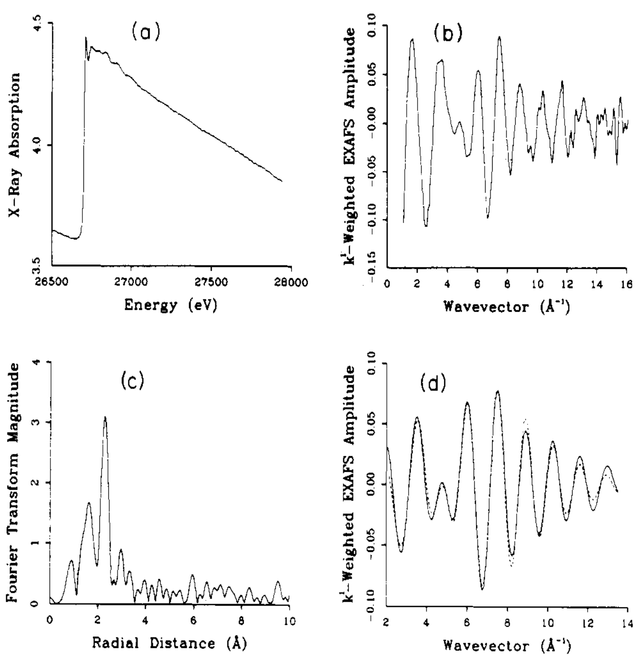

Figure 11. Analysis of the Cd K-edge EXAFS for $Cd_2(Cd_4Se_4)^{4+}$ clusters formed in the $H_{48}Na_8Y$ host: (a) X-ray absorption spectrum; (b) normalized background subtracted k^1-weighted EXAFS data; (c) Fourier transform magnitude of the EXAFS; (d) fit of inverse Fourier transformed EXAFS data using bulk CdO and CdSe reference materials.

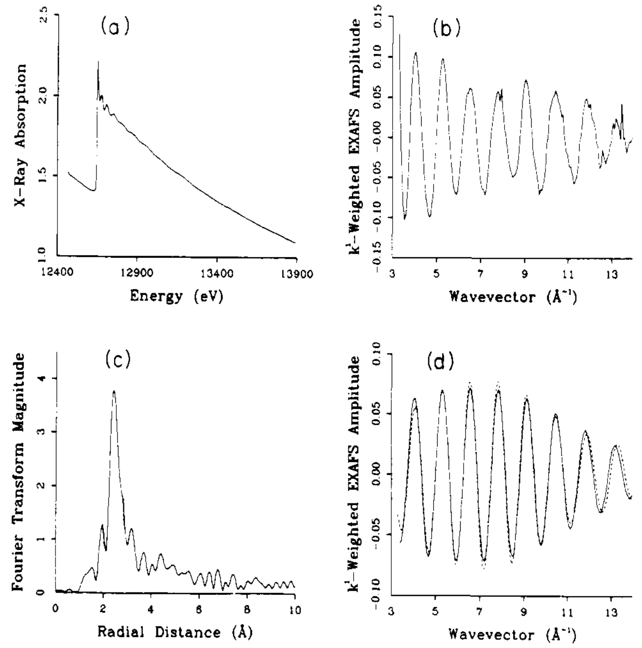

Figure 12. Analysis of the Se K-edge EXAFS for $Cd_2(Cd_4Se_4)^{4+}$ clusters formed in the $H_{48}Na_8Y$ host: (a) X-ray absorption spectrum; (b) normalized, background subtracted k^1-weighted EXAFS data; (c) Fourier transform magnitude of the EXAFS; (d) fit of inverse Fourier transformed EXAFS data using bulk CdSe reference material.

stoichiometry shown in eq 3.

These II–VI semiconductor nanocluster self-assembly reactions have also been investigated using the partially loaded $ZOMCH_3$ samples described earlier in eq 2. The reaction stoichiometry proceeds according to the following general equation:

$$n[CH_3M]H_{48-n}Na_8Y + (6-x)n/6H_2X \rightarrow [M_6X_{6-x}]_{n/6}H_{48-nx/3}Na_8Y + nCH_4 \quad (4)$$

This reaction has been studied for various samples with n = 6.3, 19.2, 37.0, and 45.1. A collection of representative mid-IR spectral traces depicting this cluster self-assembly reaction for the M = Cd, X = Se system is shown in Figure 6 for the case of n = 37.0.

The optical reflectance spectra of these encapsulated II–VI semiconductor nanoclusters convey useful information concerning the cluster self-assembly reaction and the nature of the cluster product. The nucleation and growth of the clusters can be conveniently monitored by *in situ* UV–visible reflectance spectroscopy, through the evolution of the absorption edge during the self-assembly reaction. As an example, consider the partially loaded $ZOCdCH_3$ sample having n = 37.0 as it is transformed to a cadmium selenide cluster as shown in Figure 6. Cluster formation, as monitored by *in situ* UV reflectance shown in Figure 7, is characterized by a monotonic blue shifting of the absorption edge, beginning around 400 nm and converging to a limiting value around 510 nm. The cluster product of this intrazeolite self-assembly reaction has a virtually identical absorption edge to that found for the cluster product derived from the partially loaded samples n = 6.3, 19.2, and 45.1 shown in Figure 8. In view of the relationship between cluster size and band gap (or HOMO–LUMO gap in the molecular regime) for semiconductor nanoclusters, these observations suggest considerable similarity between the clusters formed from partially loaded $ZOCdCH_3$ samples described in eq 4. The absorption edges of all of these clusters closely resemble that found for

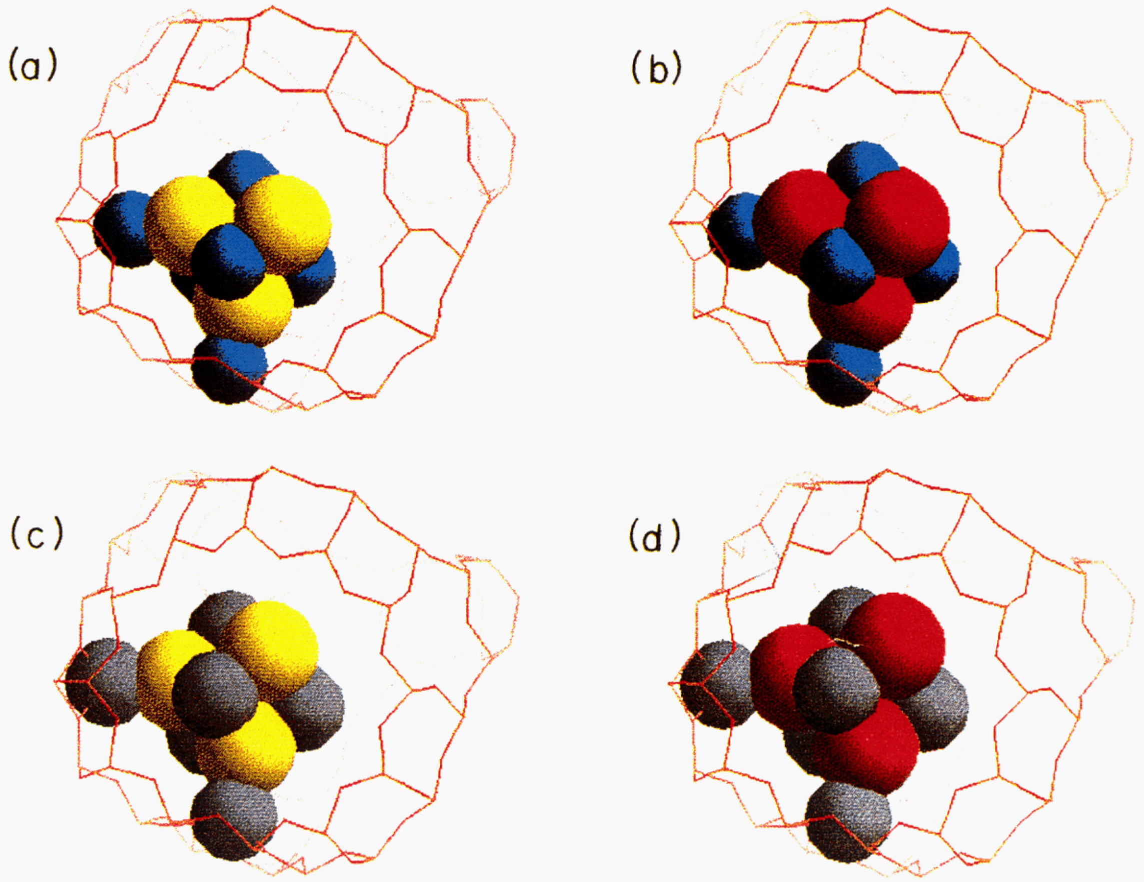

Figure 13. Model of the proposed structure of a $M_2(M_4X_4)^{4+}$ anchored cubane cluster in the α-cage of zeolite Y based on EXAFS, Rietveld refinement of PXRD, and minimum energy calculations: (a) M = Zn, X = S; (b) M = Zn, X = Se; (c) M = Cd, X = S; (d) M = Cd, X = Se.

$(Cd_6Se_4)_8H_{16}Na_8Y$ (Figure 9). These samples are shown later in this paper to contain $Cd_6Se_4^{4+}$ housed within the diamond lattice of 13-Å α-cages in the zeolite Y host. It is worth noting that from the fraction of Brønsted acid sites reinstated in the cluster self-assembly reactions described by eq 3 and shown in graphical form in Figure 10, one can determine the average stoichiometries and charges of the cluster products as listed below:

n	$Cd_6Se_{6-x}^{2x+}$	n	$Cd_6Se_{6-x}^{2x+}$
0	Cd_6Se_6	32	$Cd_6Se_{5.33}^{1.33+}$
8	Cd_6Se_6	40	$Cd_6Se_{5.17}^{1.66+}$
16	$Cd_6Se_{5.7}^{0.6+}$	48	$Cd_6Se_4^{4+}$
24	$Cd_6Se_{5.50}^{1+}$		

The noninteger stoichiometries likely signal different mixtures of Cd_6Se_6, $Cd_6Se_5^{2+}$, and $Cd_6Se_4^{4+}$ clusters in these fully loaded samples and is probably at the origin of the small differences of about 0.13 eV observed on their absorption onset energies. A similar effect and explanation also seems likely to apply to the $Cd_6Se_{6-x}^{2x+}$ clusters contained in the partially loaded samples formed according to eq 4.

EXAFS Structure Analysis of $(M_6X_4)_8H_{16}Na_8Y$, Where M = Zn, Cd; X = S, Se. The EXAFS structural analysis of the II–VI nanoclusters formed in the fully loaded $H_{48}Na_8Y$ host material is complicated by the fact that the actual cluster composition of the supercages determined by elemental analysis of numerous samples falls in the range $M_{5.0-5.5(7)}X_{3.6-4.2(6)}$ (Table 1). The EXAFS structure analysis of these fully loaded samples was found to be most consistent with an "ideal" $M_6X_4^{4+}$ cluster stoichiometry for all four cases of M = Zn, Cd and X = S, Se. The extracted bond lengths (R), coordination numbers (N), inner potentials (E_0) and Debye–Waller factors ($\Delta\sigma^2$), obtained by least-squares fitting of the desired EXAFS shell to the bulk reference compounds CdO, CdS, CdSe, ZnO, ZnS, and ZnSe, are collected together in Table 2. The EXAFS results and analysis of the four materials investigated are summarized in Figures 11 and 12. In the case of the $M_6X_4^{4+}$ clusters in zeolite Y, EXAFS is an especially valuable tool for helping to establish the local coordination environment around three of the four atom types M = Zn, Cd and X = Se. Where the probe elements exist in the same cluster, namely, $Zn_6Se_4^{4+}$ and $Cd_6Se_4^{4+}$, one has a stringent internal check for the reliability of the EXAFS analysis.

The EXAFS M–O coordination numbers and bond lengths (Table 2) are most consistent with an $M_6X_4^{4+}$ cluster tethered to the oxide framework by two M^{2+} cations. A Rietveld PXRD structure refinement of two of these cluster materials described in the following section show that one of these M^{2+} anchoring cations reside at site II in the α-cage. Considering the error of about 10–20% usually quoted for EXAFS determined coordination numbers, together with the defect nature of the supercage clusters with respect to the "ideal" $M_6X_4^{4+}$ stoichiometry, it appears that overall the M and X coordination numbers (Table 2) are more consistent with a $M_2(M_4X_4)^{4+}$ cubane cluster geometry rather than that of an $M_6X_4^{4+}$ adamantane-type cluster (the latter being a fragment building unit of the parent bulk MX semiconductor crystal lattice). Furthermore, an adamantane-like model can be eliminated

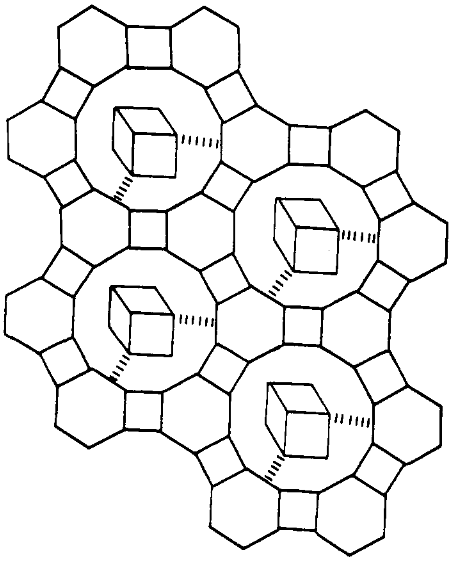

Figure 14. Schematic depiction of an ideal quantum box diamond supralattice of $M_2(M_4X_4)^{4+}$ clusters in the α-cages of a zeolite Y host.

as a viable structure for the cluster on purely spatial and geometric grounds. It is simply not possible to anchor a $M_6X_4^{4+}$ adamantane unit through two metal apices across two site II positions or site II and III positions in the α-cage (Cerius Molecular Graphics simulation). The EXAFS data are also consistent with a model of $M_2(M_4X_4)^{4+}$ clusters in every α-cage. This is determined from the absence of any detectable second M and X coordination shells in the EXAFS data. From this observation one can rule out direct interactive bonding and coupling between clusters through the 12-ring windows of the α-cage, as well as any significant contributions from II–VI semiconductor aggregates on the external surface of the zeolite (consistent with SEM and PXRD measurements). A molecular graphics representation of the $M_2(M_4X_4)^{4+}$ clusters located in the α-cage of zeolite Y, for M = Zn, Cd and X = S, Se is shown in Figure 13. These structures are consistent with the cluster stoichiometry and the EXAFS data analysis. The overall structure at the unit cell level is seen to be a lattice of α-cage encapsulated anchored cubane clusters. It is amusing to view this architecture as a "quantum box supralattice" (Figure 14). This distribution of $M_6X_4^{4+}$ clusters in the α-cage suggests that the $M_6X_5^{2+}$ and M_6X_6 clusters in the fully loaded samples formed according to eq 3 and described earlier are possibly structures in which the additional chalcogenide anions X^{2-} are capping one or two of the M^{2+} vertices of the cubane cluster and anchored to extraframework Na^+ cations in the α-cage, respectively. Further studies will be required to explore this idea.

Rietveld PXRD Structure Refinement of $(M_6X_4)_8H_{16}Na_8Y$, Where M = Zn, Cd; X = S, Se. A Rietveld refinement of low-temperature PXRD data for fully loaded Cd_6S_4-Y and Zn_6Se_4-Y samples, containing one II–VI semiconductor nanocluster per α-cage, reveals cations occupying almost one quarter of the four available six-ring site II positions. At this stage in the analysis, residual α-cage electron density associated with the second anchoring site, expected at site III, and the rest of the cluster atoms anchored by the site II and III Cd^{2+} and Zn^{2+} cations has proven difficult to find. This is likely to arise from partial occupancy of the cubane cluster amongst at least 24 possible combinations of positions in the α-cage, involving tethering to the two-site II and III M^{2+} cations. Using the proposed structure and bond lengths derived from EXAFS results for these $M_2(M_4X_4)^{4+}$ clusters, we first used Cerius Molecular Graphics to establish a likely anchoring geometry for the clusters in the supercage of zeolite Y. This showed that a M_4X_4 cubane cluster, anchored to the framework by two M^{2+} cations, must have a combination of site II and site III anchoring positions. This prediction is confirmed by the Rietveld refinement which showed occupancy at site II is equivalent to only one of these anchoring sites. Pinpointing additional anchoring locations at site III has proven difficult. This site is known to be found in three distinct crystallographic positions with a maximum multiplicity of 192. These factors are responsible for reducing the Fourier map electron intensity of cations in site III to 18 times less than that found for an equal number of cations at site II. Unfortunately, this intensity is at the level of noise in the Fourier maps, which makes further assignment difficult.

From the combined results of elemental analyses, EXAFS structural analyses and the Rietveld PXRD structure refinement, it is clear that the difficulties experienced in establishing a structure for the II–VI nanoclusters in the fully loaded $H_{48}Na_8Y$ host arise from the fact that the "ideal" $M_6X_4^{4+}$ clusters contain defects (vacancies) and also appear to be disordered in the supercages.

UV–Visible Reflectance Study of $(M_6X_4)_8H_{16}Na_8Y$, Where M = Zn, Cd; X = S, Se. Figure 9 shows a compilation of the UV–visible reflectance spectra of the four II–VI $M_6X_4^{4+}$ semiconductor nanocluster systems in zeolite Y. These spectra display three distinct features: (i) Absorption arising from the $O^{-II}(2p\pi) \rightarrow Al^{III}, Si^{IV}(3d)$ ligand-to-metal charge-transfer (LMCT) excitation of the zeolite occurs around 220 nm.[15] (ii) Absorption at lower energies, arising from $X^{-II}(3,4p\pi) \rightarrow M^{II}(4,5sp)$ LMCT excitation of the $M_6X_4^{4+}$ nanocluster, which is consistently blue shifted from the bulk MX parent semiconductor. (iii) The absorption onset of the $M_6X_4^{4+}$ clusters follow the periodic trend of bulk MX parent materials, namely $Zn_6S_4^{4+} > Zn_6Se_4^{4+} > Cd_6S_4^{4+} > Cd_6Se_4^{4+}$.

The optical spectra of II–VI $M_6X_4^{4+}$ show the blue shifted absorption edge expected for a quantum confined material. However, the component cluster sizes (<13 Å) are small compared to those of the exciton found in the parent semiconductors,[4] and their structure has changed relative to that of a fragment of the diamond lattice of the bulk II–VI materials. A molecular description for these materials in terms of a semiconductor nanocluster superlattice, rather than one of a quantum dot superlattice, is likely to be more appropriate. Further work involving, for example, electronic transport and optical measurements, as well as band structure calculations, will be required to explore the nature of these cluster supralattices in greater detail. As a first step in this direction, we have investigated the luminescence emission and excitation spectroscopy of one of these materials, namely $(Cd_6S_4)_8H_{16}Na_8Y$ over the temperature range 300–19 K.

Luminescence Spectroscopy of $(Cd_6S_4)_8H_{16}Na_8Y$. Prior to investigating the excitation and emission profiles of $Cd_6S_4^{4+}$ in zeolite Y, the luminescence behavior of the pristine $H_{48}Na_8Y$ host itself was evaluated. It was found that over the 300–19 K temperature range only a weak emission was observed around 500 nm, with a corresponding low-intensity excitation band around 260 nm. These are probably associated with various kinds of ZOH sites

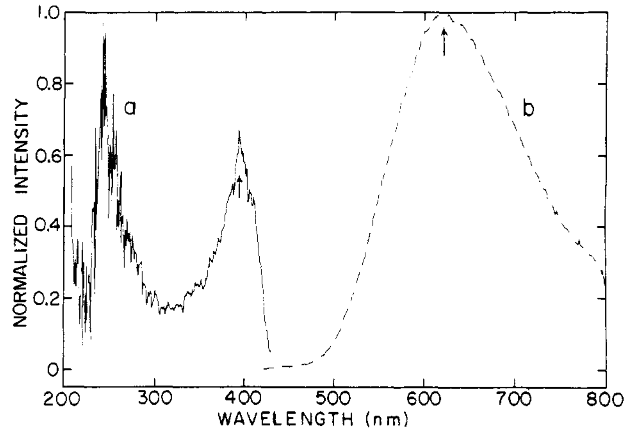

Figure 15. Normalized (a) excitation (λ_{em} = 625 nm) and (b) emission (λ_{ex} = 380 nm) spectra of $Cd_2(Cd_4S_4)^{4+}$ clusters formed in a $H_{48}Na_8Y$ host. Spectra were recorded at 19 K.

in the zeolite Y host, such as surface hydroxyls, Brønsted acid sites, and hydroxyl nests.

The most intense emission band of $Cd_6S_4^{4+}$ appears around 625 nm (λ_{ex} = 380 nm) with a fwhm ≅ 150 nm (Figure 15a). The luminescence excitation spectrum shows a band at 400 nm (λ_{em} = 625 nm) with a fwhm ≅ 80 nm (Figure 15b). The latter band is close to the absorption edge found for the same sample (Figure 9). A second excitation feature is observed around 240 nm (Figure 15b). The 400-nm feature in the excitation spectrum probably involves electron–hole pair promotion in the anchored $Cd_6S_4^{4+}$ nanoclusters, while the 240-nm band likely involves LMCT (VB → CB) excitation of the host zeolite Y. Because of the existence of improperly terminated (coordinatively unsaturated) dangling bonds on the tethered $Cd_2(Cd_4S_4)^{4+}$ cluster housed in the α-cage of zeolite Y, midgap surface states likely exist between the HOMO and LUMO orbitals of the cluster, as illustrated in Figure 16. Therefore, following excitation at 400-nm (cluster) or 240-nm (zeolite framework) the electron–hole pair can relax nonradiatively into the midgap trap states. It is believed that this process is the origin of the Stokes-shifted red luminescence observed around 625 nm in Figure 15a.

The 625-nm emission band of $Cd_6S_4^{4+}$ showed an interesting temperature dependent quenching effect (Figure 17a). The luminescence intensity gradually decreased on raising the temperature from 19 K to about 100 K. Above this temperature, the emission intensity falls off rapidly (Figure 17b). These observations follow the pattern expected for a multiphonon radiationless relaxation process.[16]

The theoretical model used in the analysis of the observed temperature dependence of the 625-nm emission band is the multiphonon radiationless relaxation model described by Fong.[16] The form of the equation and a definition of relevant terms is laid out in Figure 18. To analyze the temperature dependence of the $Cd_6S_4^{4+}$, 625-nm emission intensity, we proposed

$$I_0/I = k_{nr}/k_{nr}^{\circ}$$

where the assumption has been made that $k_{nr} \gg k_r$, which has been shown to be reasonable for quantum-confined semiconductor materials.[4,17] The resulting equation reduces to the fit of the experimental data using a nonlinear least-squares fitting of a phonon frequency ($h\nu$) and a

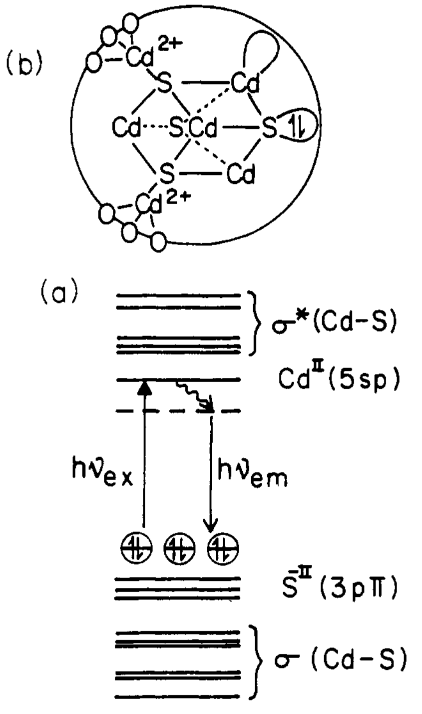

Figure 16. (a) Schematic energy level diagram depicting the HOMO (S^{-II}, 3p), LUMO (Cd^{II}, 5sp), and midgap states arising from nonterminated dangling bonds (surface states) in (b), the anchored $Cd_2(Cd_4S_4)^{4+}$ cluster located in the α-cage of zeolite Y.

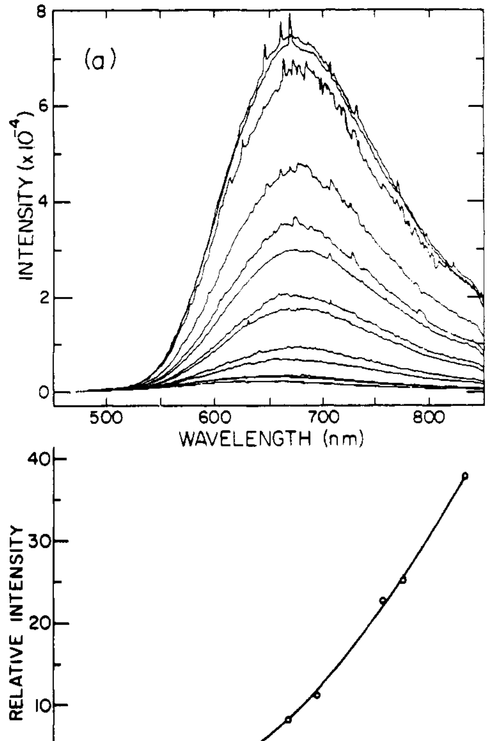

Figure 17. Temperature-dependent luminescence of $Cd_2(Cd_4S_4)^{4+}$ clusters formed in a $H_{48}Na_8Y$ host. (a) Emission spectra at T = 19, 25, 31, 39, 53, 71, 92, 105, 139, 156, 195, 207, 244, 253 °C. (b) Plot of relative intensity (I_0/I, where I_0 is the intensity of emission at 19 K) versus temperature (O) with corresponding fit using a multiphonon nonradiative decay model (—); see text.

---

(16) Fong, F. K. *Theory of Molecular Relaxation. Applications in Chemistry and Biology*; Wiley: New York, 1975.

General Expression of Radiationless Relaxation Rate k_{nr}

$$\boxed{k_{nr} = [(2\pi)^{1/2}\hbar^{-2}C] \sum_{\Delta v = -2}^{\Delta v = +2} \lambda_{\Delta v} \left[\frac{\sinh(\frac{1}{2}\beta\hbar\omega)}{G\omega^2(x^2+1)^{1/2}} \right]^{1/2} \exp\left\{ -G(2\langle n\rangle + 1) + \frac{\Delta_{\Delta v}}{\hbar\omega} \times \{\tfrac{1}{2}\beta\hbar\omega - \ln[x + (x^2+1)^{1/2}]\} + G\frac{(x^2+1)^{1/2}}{\sinh(\frac{1}{2}\beta\hbar\omega)} \right\}}$$

$\Delta_{\Delta v} = \Delta E - \Delta v\hbar\omega$ $\lambda_0 = G[6\langle n\rangle(\langle n\rangle + 1) + 1]$

$\langle n\rangle = [\exp(\beta\hbar\omega) - 1]^{-1}$ $\lambda_1 = -2G(2\langle n\rangle + 1)(\langle n\rangle + 1) + \langle n\rangle + 1$

$x = \Delta_{\Delta v}\sinh(\frac{1}{2}\beta\hbar\omega)/G\hbar\omega$ $\lambda_{-1} = -2G(2\langle n\rangle + 1)\langle n\rangle + \langle n\rangle$

$\beta = 1/kT$ $\lambda_2 = G(\langle n\rangle + 1)^2$

$S = \Delta_{\Delta v}/G\hbar\omega$ $\lambda_{-2} = G\langle n\rangle^2$

$\Delta_{\Delta v}$ = Scattered energy dissipated into phonon modes

λ_n = Electronic states differing by phonon contribution (n)

$\langle n\rangle$ = Phonon distribution function

$\hbar\omega$ = Coupling phonon frequency

G = Franck-Condon nuclear displacement parameter

C = Electronic coupling parameter

S = Effective coupling parameter; $S > 1$ (weak), $S \approx 1$ (intermediate), $S < 1$ (strong)

Figure 18. Multiphonon nonradiative decay equation with relevant terms.

Frank–Condon nuclear displacement parameter (G). The nonlinear least-squares fit was accomplished using the Levenberg–Marquardt method. Initial guesses of the parameters were made by plotting $h\nu$ versus G to find complementary values. These figures were then placed into the least-squares equation and further refined to find the best fit to the data. These results are shown in Figure 17b, where the best fit yielded 378 cm^{-1} for the average mediating phonon frequency and 42.1 for the Frank–Condon nuclear displacement parameter. Qualitatively, a higher thermal quenching temperature corresponds to a higher frequency phonon mode participating in the nonradiative relaxation pathway. These results depict the intermediate coupling case with a value for the electron–phonon coupling parameter, S, of close to unity. In this regime, many mediating phonons contribute to quenching, with the fitted frequency representing an average of the participating modes.

Possible vibrational modes that could contribute to this average phonon frequency of 378 cm^{-1} are a combination of both $Cd_6S_4^{4+}$ cluster skeletal modes (cf. the bulk CdS phonon frequency is about 270 cm^{-1}) and δTO_4 deformation and pore-opening modes of the zeolite, which occur in the regions of 500 and 300 cm^{-1}, respectively.[18] These results are consistent with a structural model involving the $Cd_6S_4^{4+}$ cluster anchored in the α-cage of the zeolite host. Similar conclusions emerged from a study of β-cage encapsulated $Cd_4(S/O)_4$ cube clusters obtained by H_2S exposure to ion-exchanged CdY.[4] The literature on II–VI semiconductor clusters (including ZnS and CdS clusters made by arrested precipitation, as well as CdS clusters in Nafion films) show that electron–phonon coupling is a commonly occurring theme in the temperature dependence of the luminescence of these materials.[19] Note that the assumption $k_{nr} \gg k_r$ is true only when the fluorescence yield of the sample is low. This appears to be the case for the $Cd_6S_4^{4+}$ clusters in zeolite Y over the studied temperature range 19–300 K. More work needs to be carried out to investigate this point, as well as a range of other photophysical aspects of the system.

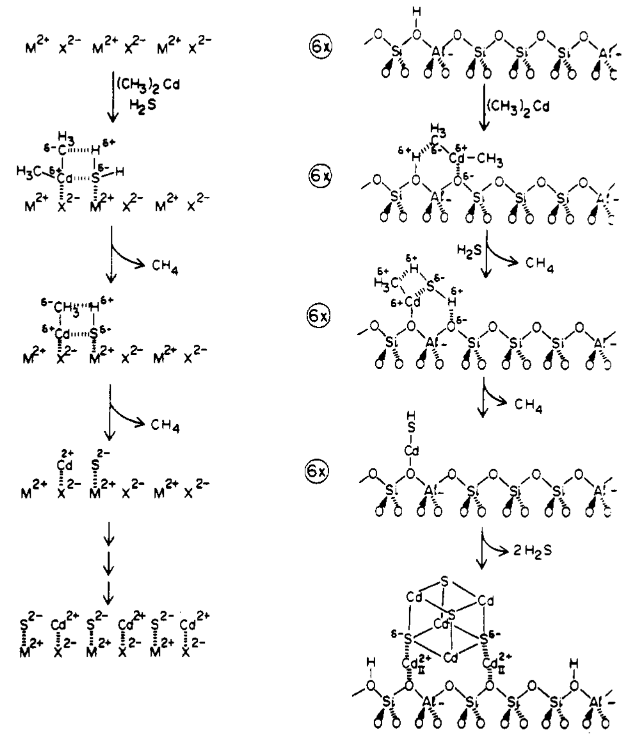

Figure 19. Schematic illustration of (a) epitaxial formation of a CdS thin film on a II–VI bulk semiconductor MX surface and (b) topotactic formation of $Cd_6S_4^{4+}$ clusters on the curved internal surface of zeolite Y.

Epitactic and Topotactic MOCVD Deposition of II–VI Semiconductors. It is instructive to compare the process of depositing, from MOCVD precursors, epitaxial layers of a II–VI semiconductor on a 2-D planar substrate (e.g., heteroepitaxy of say CdS on a II–VI MX single-crystal material) with that of the intrazeolite topotactic procedure of assembling a II–VI semiconductor nanocluster lattice on the 3-D curved internal surface of a zeolite (e.g., $Cd_6S_4^{4+}$ in the diamond lattice of 13-Å α-cages of zeolite Y).

In terms of overall reaction stoichiometry, the epitaxial MOCVD process can be described according to eq 5. In

$$MX + H_2S + (CH_3)_2Cd \rightarrow (MX)CdS + 2CH_4 \quad (5)$$

this "single-step" chemical vapor deposition experiment, the layer-forming reaction is driven to completion thermally at elevated temperatures of around 400 °C.[20] This deposits CdS and evolves gaseous CH_4 as byproduct. Likely surface species involving MOCVD precursors and the MX substrate are illustrated in Figure 19a. This

---

(17) Chestnoy, N.; Hull, R.; Brus, L. E. *J. Chem. Phys.* **1986**, *85*, 2237–2242. O'Neil, M.; Marohn, J.; McLendon, G. *J. Phys. Chem.* **1990**, *94*, 4356–4363.

(18) Flanigen, E. M. In *Zeolite Chemistry and Catalysis, A.C.S. Monograph 171*; **1976**, Rabo, J. A., Ed.; American Chemical Society: Washington, D.C., pp 80–117. Blackwell, C. S. *J. Phys. Chem.* **1979**, *83*, 3257.

(19) Chestnoy, N.; Harris, T. D.; Hull, R.; Brus, L. E. *J. Phys. Chem.* **1986**, *90*, 3393. Wang, Y.; Suna, A.; McHugh, J.; Hilinski, E. F.; Lucas, P. A.; Johnson, R. D. *J. Chem. Phys.* **1990**, *92*, 6927.

(20) Stringfellow, G. B. *Organometallic Vapor-Phase Epitaxy: Theory and Practice*; Academic Press: Boston, 1989; p 115.

scheme takes due cognizance of the charges on the M^{2+} and X^{2+} surface sites, as well as the charge polarities of the H_2S and $(CH_3)_2Cd$.

By comparison, the topotactic MOCVD process is a "two-step" chemical vapor deposition experiment, consisting first of precursor anchoring according to eq 6. This occurs

$$6ZOH + 6(CH_3)_2Cd \rightarrow 6ZOCdCH_3 + 6CH_4 \quad (6)$$

exclusively in the α-cage of zeolite Y and is driven to completion at room temperature, by reactive anchoring involving α- and β-cage Brønsted acid sites and nucleophilic methyl groups of $(CH_3)_2Cd$. Gaseous CH_4 is evolved as a by-product. Thus in $H_{48}Na_8Y$, a fully loaded product locates $6ZOCdCH_3$-anchored MOCVD-type precursors in the α-cage, which are set for reaction with H_2S and cluster self-assembly according to eq 7 and 8. Note that charge

$$6ZOCdCH_3 + 6H_2S \rightarrow \{6ZOCdSH\} + 6CH_4 \quad (7)$$

$$\{6ZOCdSH\} \rightarrow 4ZOCd_6S_4 + 2H_2S + 2ZOH \quad (8)$$

balance with the zeolite framework, as well as spatial and compositional homogeneity throughout the zeolite crystal lattice is precisely maintained in the reactions shown in eqs 6–8.

The results of this cluster assembly study, as well as those of a previous report in which we focused attention on MOCVD precursor anchoring,[9] allow us to propose a *reaction scheme for the entire two-step topotactic* MOCVD process according to that illustrated in Figure 19b. In essence, a "zeolate ligand" type of coordination site captures $(CH_3)_2Cd$ in the first step, allowing it to react with a nearby Brønsted acid site to produce anchored $ZOCdCH_3$ species in sites II and III of the α-cage. These then participate in the second-step reaction in which the "zeolate ligand" organizes anchored $ZOCdCH_3$ and adsorbed H_2S in an adjacent fashion, as illustrated in Figure 19b. This yields {ZOCdSH} hydrosulfide reactive intermediates. Six of these {ZOCdSH} species occupying α-cage sites participate in a cluster self-assembly reaction, constrained and templated by the "zeolate ligand" to form $Cd_6S_4^{4+}$ nanoclusters in every α-cage of the zeolite Y host (Figure 19b). The concept of capping improperly terminated surface sites in II–VI semiconductor clusters with ligands such as phenylate and phenylthiolate is analogous with the proposed form of "zeolate ligand" capping. This serves multiple roles including stabilizing the cluster to further agglomeration and removing some surface states associated with dangling bonds from their midgap positions.

Acknowledgment. We wish to thank the Natural Sciences and Engineering Research Council of Canada's Operating and Strategic Grants Programs for financial support of this work. M.R.S. acknowledges NSERC and OGS for graduate scholarship support during the course of this work. The low-temperature PXRD and EXAFS measurements were carried out at the National Synchrotron Light Source, Brookhaven National Laboratories, which is supported by the US Department of Energy, Division of Materials Sciences and the Division of Chemical Sciences. We wish to thank Dr. David Cox for his assistance at Brookhaven National Laboratories. We also would like to thank our colleagues at the University of Toronto for invaluable discussions during the course of this work.